

Inferring the origins of the pulsed γ -ray emission from the Crab pulsar with ten-year *Fermi* LAT data

Paul K. H. Yeung¹

Institute for Experimental Physics, Department of Physics, University of Hamburg, Luruper Chaussee 149, D-22761 Hamburg, Germany
e-mail: kin.hang.yeung@desy.de

Received April 14, 2020; accepted June 6, 2020

ABSTRACT

Context. The Crab pulsar is a bright γ -ray source detected at photon energies up to ~ 1 TeV. Its phase-averaged and phase-resolved γ -ray spectra below 10 GeV exhibit exponential cutoffs while those above 10 GeV apparently follow simple power-laws.

Aims. We re-visit the γ -ray properties of the Crab pulsar with 10-year *Fermi* Large Area Telescope (LAT) data in the range of 60 MeV–500 GeV. With the phase-resolved spectra, we investigate the origins and mechanisms responsible for the emissions.

Methods. The phaseograms are reconstructed for different energy bands and further analysed using a wavelet decomposition. The phase-resolved energy spectra are combined with the observations of ground-based instruments like MAGIC and VERITAS to achieve a larger energy coverage. We fit power-law models to the overlapping energy spectra from 10 GeV to ~ 1 TeV. We include in the fit a relative cross-calibration of energy scales between air-shower based gamma-ray telescopes with the orbital pair-production telescope of the *Fermi* mission.

Results. We confirm the energy-dependence of the γ -ray pulse shape, and equivalently, the phase-dependence of the spectral shape for the Crab pulsar. A relatively sharp cutoff at a relatively high energy of ~ 8 GeV is observed for the bridge-phase emission. The $E > 10$ GeV spectrum observed for the second pulse peak is harder than those for other phases.

Conclusions. In view of the diversity of phase-resolved spectral shapes of the Crab pulsar, we tentatively propose a multi-origin scenario where the polar-cap, outer-gap and relativistic-wind regions are involved.

1. Introduction

The Crab pulsar and its nebula are products of the supernova explosion SN1054 and act as powerful particle accelerators. The Crab pulsar is one of the 239 pulsars whose γ -ray pulsations have been significantly detected with the on-board *Fermi* Large Area Telescope (LAT; The *Fermi*-LAT collaboration 2019). Also, it is the only pulsar with pulsed emissions above 100 GeV robustly confirmed by the ground-based instruments MAGIC and VERITAS (e.g., VERITAS Collaboration et al. 2011; Aleksić et al. 2012). Recently, pulsed emission has been detected even up to TeV energies from the Crab pulsar (Ansoldi et al. 2016).

The relevant emission mechanisms of γ -rays from pulsars are still under investigation. There have been a number of particle acceleration sites proposed as origins of pulsed γ -ray emission. The first one proposed is the polar cap region confined in the open magnetosphere at low altitudes (Sturrock 1971; Harding et al. 1978; Daugherty & Harding 1982). Due to rapid pair-creations under strong magnetic field, polar cap models predict a sharp super-exponential cutoff at several GeV which is not consistent with the observed γ -ray spectra of pulsars (Abdo et al. 2013).

The second and third proposed regions are both located at high altitudes in the outer magnetosphere, respectively the slot gap (along the last open magnetic field lines; Arons 1983; Dyks & Rudak 2003; Muslimov & Harding 2004) and outer gap (extending to the edge of the light cylinder; Cheng et al. 1986; Romani & Yadigaroglu 1995; Cheng et al. 2000; Takata et al. 2006). The *Fermi* LAT pulse profiles and spectra of pulsars demonstrate that the responsible high-energy electron beams have a fan-like geometry scanning over a large fraction of the outer magneto-

sphere (Abdo et al. 2013). This favours the outer gap emission as a generally dominant component.

As observed with *Fermi* LAT, MAGIC and VERITAS, at most on-pulse phases, the Crab pulsar's spectrum above 10 GeV follows a rather hard power-law tail which extends beyond hundreds of GeV (Aleksić et al. 2014; Nguyen & VERITAS Collaboration 2015; Ansoldi et al. 2016). This certainly disfavors domination by the magnetospheric synchrotron-curvature mechanism, whose spectrum is theoretically expected to be well characterised by an exponential cutoff at several GeV due to magnetic pair-creations and/or radiation losses (Cheng et al. 1986; Romani 1996; Muslimov & Harding 2004; Takata et al. 2006; Tang et al. 2008). On the other hand, it is put forward by Harding & Kalapotharakos (2015) that magnetospheric synchrotron-self-Compton (SSC) emission from leptonic pairs generated by cascades can account for the GeV spectral properties observed for the Crab pulsar.

In addition, the fourth particle acceleration site, which is the relativistic wind located outside the light cylinder, is proposed as a responsible region as well (Bogovalov & Aharonian 2000; Aharonian & Bogovalov 2003; Aharonian et al. 2012). It is more recently suggested that the highest energy pulsed emission could be produced in the region of the current sheet at a distance of 1–2 light cylinder radii (Harding et al. 2018) or even extending to tens of light cylinder radii (Arka & Dubus 2013; Mochol & Petri 2015), where the kinetic-energy dominated wind is assumed to be launched.

It is noteworthy that the Crab pulsar has an energy-dependent γ -ray pulse shape, and equivalently, a phase-dependent spectral shape (e.g., Fierro et al. 1998; Abdo et al. 2010; DeCesar 2013).

arXiv:2004.07669v3 [astro-ph.HE] 10 Mar 2021

This may suggest that emissions at different pulse phases are dominated by different emission regions.

In this work, we re-visit the γ -ray phaseograms and phase-resolved spectral energy distributions (SEDs) of the Crab pulsar, with the >60 MeV LAT data accumulated over ~ 10 years. Considering our LAT results in context with observations of ground-based instruments, we discuss the γ -ray origins for different phases individually.

2. Data reduction & analysis

We perform a series of binned maximum-likelihood analyses (with an angular bin size of 0.1°) for a region of interest (ROI) of $30^\circ \times 30^\circ$ centered at RA= $05^h 34^m 31.94^s$, Dec= $+22^\circ 00' 52.2''$ (J2000), which is approximately the radio center of the Crab Nebula (Lobanov et al. 2011). We use the data of 60 MeV–500 GeV photon energies, registered with the LAT between 2008 August 4 and 2018 August 20. The data are reduced and analyzed with the aid of the *Fermi* Science Tools v11r5p3 package.

Considering that the Crab Nebula is quite close to the Galactic plane (with a Galactic latitude of -5.7844°), we adopt the events classified as Pass8 “Clean” class for the analysis so as to better suppress the background. The corresponding instrument response function (IRF) “P8R2_CLEAN_V6” is used throughout the investigation. We further filter the data by accepting only the good time intervals where the ROI was observed at a zenith angle less than 90° so as to reduce the contamination from the albedo of Earth. In phase-resolved analyses, we adopt the timing solution of the Crab pulsar provided by M. Kerr.

In order to account for the contribution of diffuse background emission, we include the Galactic background (gll_iem_v06.fits), the isotropic background (iso_P8R2_CLEAN_V6_v06.txt) as well as all other point sources cataloged in the LAT 8-year Point Source Catalog (4FGL; The Fermi-LAT collaboration 2019) within 32° from the ROI center in the source model. We set free the spectral parameters of the sources within 10° from the ROI center (including the prefactor and index of the Galactic diffuse background as well as the normalization of the isotropic background) in the analysis. For the sources at angular separation beyond 10° from the ROI center, their spectral parameters are fixed to the catalog values.

The three point sources located within the nebula are cataloged as 4FGL J0534.5+2200, 4FGL J0534.5+2201i, and 4FGL J0534.5+2201s, which model the Crab pulsar, the IC, and synchrotron components of the Crab Nebula, respectively. In some cases, we fix the parameters of one or two components or even remove them from the source model, so as to avoid degeneracies in the fitting procedure.

3. Results

3.1. LAT phaseograms at different energies

First of all, we look into the LAT pulse profiles of the Crab pulsar in four energy bands: 60–600 MeV, 0.6–6 GeV, 6–60 GeV, and 20–500 GeV. We divide the full-phase into 50 bins (i.e., each bin covers a phase interval of 0.02). In the maximum-likelihood analysis for each bin, we remove 4FGL J0534.5+2201i and 4FGL J0534.5+2201s from the source model, and assign a single power-law (PL) to 4FGL J0534.5+2200 (i.e., the total emission of the Crab pulsar and its nebula is modelled as one component here). We adopt the same convention of phase as in Buehler et al. (2012).

Table 1. Pulse peak phases determined from LAT phaseograms.

Energy Band (GeV)	Peak 1 ^a	Peak 2 ^b
0.06–0.6	0.997 ± 0.004	0.393 ± 0.004
0.6–6	0.998 ± 0.004	0.389 ± 0.005
6–60	0.998 ± 0.004	0.391 ± 0.005
20–500	0.003 ± 0.006	0.392 ± 0.004

^a It is calculated as the arithmetic mean of phases in 0.98–0.02 weighted by relative fluxes.

^b It is calculated as the arithmetic mean of phases in 0.36–0.42 weighted by relative fluxes.

The preliminary phaseograms show the first peak within the phase range of 0.98–0.02 and the second peak within phase 0.37–0.41. In order to localise the two peaks, we sub-divide phase 0.98–0.02 and 0.37–0.41 into bins of 0.01 phase interval, and then further sub-divide phase 0.99–0.01 and 0.38–0.40 into even smaller bins of 0.005 phase interval. Phase 0.58–0.88 is taken as the off-pulse region (thereafter OFF) where we determine the un-pulsed nebular fluxes. In each phaseogram, we combine those bins within OFF into 1 bin and then subtract the determined nebular flux from all bins, such that the flux within OFF is set at 0. The finalised phaseograms are plotted in Figure 1, together with the >85 GeV phaseogram observed by VERITAS (Nguyen & VERITAS Collaboration 2015). The phase-averaged flux in each energy band we investigate is also overlaid in the phaseogram.

Comparing all LAT phaseograms presented here, we have no evidence for any phase shift of the two peaks ($< 1\sigma$; see Table 1). According to the pulse shapes, we divide the on-pulse region into 7 phase ranges for detailed analyses: Phase 0.88–0.96 (the leading wing of the first pulse; LW1), 0.96–0.02 (the peak region of the first pulse; P1), 0.02–0.12 (the trailing wing of the first pulse; TW1), 0.12–0.20 (the bridge between two pulses; BD), 0.20–0.36 (LW2), 0.36–0.42 (P2) and 0.42–0.58 (TW2).

In 60–600 MeV and 0.6–6 GeV, the ratios of maximum fluxes of P1 to P2 are 2.60 ± 0.05 and 2.85 ± 0.08 , respectively. This ratio greatly decreases to 1.54 ± 0.23 in 6–60 GeV and to 1.14 ± 0.59 in 20–500 GeV. It further drops to an even smaller value of 0.57 ± 0.09 in the >85 GeV band.

From 60–600 MeV to 0.6–6 GeV, the fractional flux of BD increases from $(1.82 \pm 0.09)\%$ to $(3.15 \pm 0.07)\%$. This fraction further rises to $(8.38 \pm 0.73)\%$, $(4.7 \pm 4.4)\%$ and $(11.1 \pm 4.2)\%$ in 6–60 GeV, 20–500 GeV and >85 GeV respectively.

3.2. Wavelet analyses on LAT phaseograms

At any photon energy, the flux of the Crab pulsar changes exponentially during the wing phases. In order to investigate the instantaneous rates of flux change at different phases and energies, we apply continuous wavelet transforms to the preliminary LAT phaseograms which have a uniform bin size of a 0.02 phase interval. The Ricker wavelet is adopted. The photon statistics above 20 GeV are not sufficient for the wavelet transform. The results are shown in Figure 2.

The wavelet scale represents the timescale of flux change. Overall, at higher energies, the wavelet components at LW1 and TW2 extend to lower wavelet scales and become closer to vertical, while the components at TW1, LW2 and BD have greater power indices and become more tightly connected with each other.

Considering the pulse profiles and wavelet transformations synthetically, we derive a number of general trends: As the photon energy increases,

- (a) the rate of flux increase in LW1 becomes faster, leading to a narrower wing;
- (b) the rate of flux decrease in TW1 becomes slower, leading to a broader wing;
- (c) the rate of flux increase in LW2 becomes slower, leading to a broader wing;
- (d) the rate of flux decrease in TW2 becomes faster, leading to a narrower wing;
- (e) the flux ratio of P1 to P2 drops;
- (f) the fractional flux of BD rises.

The trends (a), (d) and (e) confirm what was reported in Abdo et al. (2010). In the following sub-sections, we further examine the trends (a)–(f) with spectral analyses.

3.3. LAT SEDs for different pulse phases

3.3.1. Scheme of spectral analyses

In broadband spectral analyses, we enable the energy dispersion correction which operates on the count spectra of most sources including the entire Crab pulsar/nebula complex, following the recommendations of the *Fermi* Science Support Center.

The energy spectrum of the un-pulsed nebular emission in the 60 MeV–100 GeV band is reconstructed by fitting a two-component (additive) model to the data collected during OFF. The flux normalisation of the pulsar component is fixed at 0. Similar to previous studies (Buehler et al. 2012; Yeung & Horns 2020), we assign the synchrotron component a PL with a photon index constrained within 3–5, and assign the IC component a log-parabola (LP):

$$\frac{dN}{dE} = N_0 \left(\frac{E}{10 \text{ GeV}} \right)^{-(\alpha + \beta \ln(E/10 \text{ GeV}))},$$

where α is constrained within 0–2. It turns out that the synchrotron component has a PL index of 3.427 ± 0.019 and an integrated flux of $(2.500 \pm 0.018) \times 10^{-6}$ ph cm $^{-2}$ s $^{-1}$ in the full phase, while the LP parameters of the IC component are determined to be $\alpha = 1.759 \pm 0.023$, $\beta = 0.106 \pm 0.014$ and $N_0 = (5.12 \pm 0.14) \times 10^{-13}$ cm $^{-2}$ s $^{-1}$ MeV $^{-1}$ (scaled to the full phase).

Then, we apply this nebular model to reconstruct the pulsar spectra at different phases in the same energy band. We examine how well the pulsar spectrum at each phase is described by, respectively, a power law with a super-/sub-exponential cutoff (PLSEC):

$$\frac{dN}{dE} = N_0 \left(\frac{E}{E_0} \right)^{-\Gamma} \exp\left[-\left(\frac{E}{E_c}\right)^\lambda\right],$$

and a power law with an exponential cutoff (PLEC) where λ in PLSEC is fixed at 1. The pulsar parameters are left free while the nebular parameters are fixed at the determined values (with proper scalings to flux normalisations according to phase intervals). The obtained spectral models for the pulsar are tabulated in Table 2. The phase-averaged pulsar spectrum is plotted with the nebular spectrum in Figure 3, and the phase-resolved pulsar spectra are plotted in Figure 4. Each presented flux has been scaled by the inverse of the phase interval (i.e., it refers to as the flux per unit phase). The spectral parameters for individual phase bins of 0.04 are plotted in Figures 5 & 6.

We repeat this chain of exercise for the 10–500 GeV band. For the nebular emission, the synchrotron component is negligible, so we remove it from the source model. The nebular IC

component is still modelled as a LP, while the pulsar component is modelled as a PL. The best-fit parameters for the nebula are $\alpha = 1.86 \pm 0.14$, $\beta = 0.023 \pm 0.047$ and $N_0 = (5.10 \pm 0.42) \times 10^{-13}$ cm $^{-2}$ s $^{-1}$ MeV $^{-1}$ (scaled to the full phase). The results are tabulated in Table 3 and are overlaid in Figures 3 & 4. We also examine how significant the improvement is when we assign a curved model to the pulsar spectrum. Since the photon index at BD appears to be higher, we adjust the phase width of BD and study the evolution of the photon index (Figure 7). The narrowest phase width of BD we investigate is 0.05 for which the Crab pulsar is detected at a $\sim 4\sigma$ significance.

We proceed to generate binned spectra for the nebula and pulsar. We divide the 60 MeV–6 GeV band into 12 discrete energy bins (six bins per decade). 6–10 GeV is the 13th bin. The 10–500 GeV band is divided into five discrete bins, the first of which is further split into two. The procedures of broadband fittings are also applied to the spectral fittings of each bin. The nebular emission in each bin is modelled as a PL with an index fixed at a value derived from the broadband fitting. The results are overlaid in Figures 3 & 4 as well.

Based on the binned spectra, we compute the pulsed fraction of the entire Crab pulsar/nebula complex, as well as the pulsar flux ratios between different pairs of phases at energies from 60 MeV to 100 GeV (plotted in Figure 8). The pulsed fraction is defined as $(F_{max} - F_{min}) / (F_{max} + F_{min})$, where F_{min} is the nebular flux, and F_{max} is the pulsar flux in either P1 or P2 (the higher one) added to the nebular flux.

3.3.2. Summary of spectral properties

The pulsed fraction of the entire Crab pulsar/nebula complex is strongly dependent on the photon energy (see Figure 8). It is $\geq 90\%$ (and $\geq 80\%$) in 0.2–4 GeV (and 0.1–8 GeV). It drops to 25–50% in 20–100 GeV.

For the phase-averaged pulsar spectrum in 60 MeV–100 GeV, a PLSEC with $\lambda \approx 0.31$ fits the data better than PLEC, indicating that a sub-exponential cutoff is strongly favoured. It is comforting to see that, in 0.2–14 GeV, this PLSEC model agrees within 15% with the 4FGL model reconstructed with fixing λ at 2/3. The λ values are widely varying with the pulse phase (see Figure 6 and Table 2). Noticeably, during the phase 0.04–0.28, λ is consistent with 1 within the tolerance of statistical uncertainties and PLSEC is not significantly preferred over PLEC ($\leq 1\sigma$). In a PLSEC model, there is a strong correlation of λ with any other parameter, making it nonsense to compare their values among different phases. Instead, we compare the Γ and E_c values of PLEC models among different phases.

The PLEC model for the full-phase spectrum has a photon index $\Gamma \approx 1.85$ and a cutoff energy $E_c = 4.3 \pm 0.1$ GeV. During the phase 0.08–0.36 (and 0.16–0.28), PLEC fittings yield harder Γ of ≤ 1.7 (and ~ 1.45). During the phase 0.04–0.16 and 0.16–0.24, E_c of PLEC is as high as ~ 10.5 GeV and ~ 6 GeV, respectively (see Figure 5). These indicate that the total fractional flux of TW1, BD and LW2 generally increases with the photon energy. As follows, we summarise the <10 GeV spectral properties of the Crab pulsar based on PLEC and binned spectra (see Figures 3, 4 & 8 as well as Table 2), and relate them to the trends (a)–(f) derived in §3.2.

- The Γ value at LW1 is lower than that at P1 by 0.07 ± 0.02 . On the other hand, the E_c value at LW1 is about 40% of that at P1. The flux ratio of LW1 to P1 is strongly decreasing in 0.5–10 GeV, confirming the trend (a).

Table 2. 60 MeV–100 GeV spectral properties of the Crab pulsar at different phases.

Phase	PLEC		Γ	E_c (MeV)	PLSEC		$F(60 \text{ MeV}–100 \text{ GeV})^a$ ($10^{-6} \text{ cm}^{-2} \text{ s}^{-1}$)	ΔTS^b
	Γ	E_c (MeV)			λ			
Full-phase	1.851 ± 0.004	4259 ± 80	1.328 ± 0.006	38.1 ± 1.5	0.308 ± 0.002	3.10 ± 0.01	512	
LW1	1.757 ± 0.021	1137 ± 55	0.888 ± 0.026	9.53 ± 0.76	0.351 ± 0.005	3.11 ± 0.03	32.1	
P1	1.827 ± 0.005	2750 ± 51	0.870 ± 0.007	0.51 ± 0.01	0.238 ± 0.001	22.93 ± 0.07	609	
TW1	1.831 ± 0.010	9181 ± 626	1.790 ± 0.033	7349 ± 1594	0.791 ± 0.122	2.64 ± 0.03	3.2	
BD	1.507 ± 0.032	7792 ± 922	1.501 ± 0.078	7607 ± 2522	0.979 ± 0.244	0.56 ± 0.03	0.01	
LW2	1.634 ± 0.010	4646 ± 175	1.500 ± 0.040	2244 ± 564	0.658 ± 0.062	2.38 ± 0.02	27.7	
P2	1.911 ± 0.006	6129 ± 259	1.660 ± 0.074	708 ± 612	0.415 ± 0.068	10.03 ± 0.06	93	
TW2	1.954 ± 0.026	1870 ± 164	1.029 ± 0.036	0.97 ± 0.09	0.256 ± 0.003	1.36 ± 0.02	17.7	

^a The integrated flux per unit phase.

^b The difference in test-statistic (TS) between PLSEC and PLEC. Its square root is the significance at which PLSEC is preferred over PLEC.

Table 3. 10–500 GeV spectral properties of the Crab pulsar at different phases.

Phase	PL Γ	$F(10\text{-}500 \text{ GeV})^a$ ($10^{-9} \text{ cm}^{-2} \text{ s}^{-1}$)	TS
Full-phase	3.33 ± 0.15	2.90 ± 0.14	698.9
LW1	4.66 ± 0.63	<0.69	0.4
P1	3.47 ± 0.26	9.18 ± 0.79	319.7
TW1	3.45 ± 0.29	5.68 ± 0.53	235.7
BD	4.26 ± 0.59	3.82 ± 0.53	114.5
LW2	3.31 ± 0.25	4.64 ± 0.40	256.8
P2	2.84 ± 0.18	10.64 ± 0.84	354.4
TW2	2.85 ± 1.06	<0.97	4.0

^a The integrated flux per unit phase.

- Γ at TW1 and that at P1 are consistent with each other within the tolerance of statistical uncertainties, and E_c at TW1 is three times higher than that at P1. The flux ratio of TW1 to P1 is strongly increasing in 0.5–10 GeV, confirming the trend (b).
- Γ at LW2 is significantly lower than that at P2 by 0.28 ± 0.01 . On the other hand, E_c at LW2 is about three-fourth of that at P2. At ~ 250 MeV, the flux ratio of LW2 to P2 starts rising with the photon energy significantly. This increment might come to an end at >4 GeV. Hence, we have strong evidence for the validity of the trend (c) in 0.25–4 GeV.
- Γ at TW2 is consistent with that at P2 (the difference is only at a $\sim 1.6\sigma$ significance), and E_c at TW2 is approximately 30% of that at P2. At ~ 350 MeV, the flux ratio of TW2 to P2 starts dropping with the photon energy significantly. This decrement might come to an end at >2 GeV. Hence, we have strong evidence for the validity of the trend (d) in 0.35–2 GeV.
- Both the Γ values at P1 and P2 closely match the one for the full phase (the differences are $\lesssim 0.06$). E_c at P1 is about two-third of that for the full phase, which is about two-third of that at P2. In 60 MeV–1.5 GeV, the fractional flux of P1 is essentially uniform (the percent variance between any two bins is $\lesssim 20\%$). Above 1.5 GeV, the fractional flux of P1 starts dropping with the photon energy. On the other hand, the fractional flux of P2 remains uniform at energies between 60 MeV and 10 GeV. Hence, the trend (e) is manifested in 1.5–10 GeV.
- BD has the lowest Γ value among all phases we investigate. It is much lower than Γ for the full phase by 0.34 ± 0.03 . Also, E_c at BD is higher than that for the full phase by a factor

of ~ 1.8 . The fractional flux of BD is robustly increasing in 0.35–10 GeV, confirming the trend (f).

In 10–500 GeV, a PL is sufficient to describe the pulsar spectrum at each phase, and likelihood ratio tests indicate that any curved models are not statistically required ($\lesssim 1\sigma$). Therefore, the energy-dependence of a flux ratio between two phases above 10 GeV can be directly inferred from their difference in photon index (see Table 3). Exceptionally, the detection significance of the Crab pulsar at LW1 and TW2 is too low ($< 2\sigma$) so that the “ad hoc” PL models for these two phases cannot precisely predict the pulsar’s differential flux. The photon indices of the Crab pulsar for P1 and TW1 are consistent with each other within the tolerance of statistical uncertainties. The indices for LW2 and P2 are consistent with each other within the tolerance of 1.5σ uncertainties. Therefore, we have no robust evidence for the validities of the trends (a)–(d) at energies above 10 GeV.

Interestingly, while the <3 GeV spectrum of the Crab pulsar is hardest at BD, its >10 GeV spectrum is apparently softest at BD. This is consistent with the relatively sharp cutoff of the BD spectrum reported in Table 2. During the phase 0.135–0.185 (a central interval of BD), the fractional flux drops as $E^{-2.6 \pm 1.2}$ at a $\sim 3\sigma$ significance (see Figure 7), indicating a potential reverse of the trend (f) above 10 GeV.

The validity of the trend (e) above 10 GeV is examined in the next sub-section with joint fits of the LAT and ground-based instruments’ spectral points.

3.4. Comparing LAT spectra to observations of ground-based instruments

It is interesting to join the spectral data of LAT and ground-based instruments together for comparisons. Before that, we adjust the phase ranges of the two peaks to be the same as those defined in Ansoldi et al. (2016) (Phase 0.983–0.026 and 0.377–0.422; thereafter $P1_M$ and $P2_M$ respectively). For these two phase ranges, we follow the same scheme to re-compute the LAT fluxes of the Crab pulsar in different energy bins starting from 10 GeV, which are plotted with the MAGIC fluxes in Figure 9. For the full-phase, the LAT and VERITAS fluxes of the Crab pulsar at >10 GeV (the latter is taken from Nguyen & VERITAS Collaboration (2015)) are overlaid in Figure 9 as well.

It is clearly demonstrated that the phase-averaged VERITAS fluxes at energies above 80 GeV are higher than the extrapolated fluxes of the PLSEC fit to the broadband LAT spectrum. Also, for each phase interval we investigate here, a PL is sufficient

to describe the spectrum between 10 GeV and ~ 1 TeV, and a spectral curvature or break is not statistically required ($< 1\sigma$).

In order to take into account the differences in energy scale among LAT, MAGIC and VERITAS, we fit the data set of each phase to a power law with a scaling factor on photon energies measured by ground-based instruments (PLSF):

$$\frac{dN}{dE} = \begin{cases} N_0 \left(\frac{E}{50 \text{ GeV}} \right)^{-\Gamma} & \text{for LAT data} \\ N_0 \left(\frac{\epsilon E}{50 \text{ GeV}} \right)^{-\Gamma} & \text{for data of ground-based instruments} \end{cases}$$

Since the data for $P1_M$ and $P2_M$ is collected by the same ground-based instrument, their data sets are fit together such that their solutions share the same scaling factor ϵ . The results of fittings are presented in Table 4 and the best-fit model lines are overlaid in Figure 9.

It is worth mentioning that the ϵ values obtained for MAGIC and VERITAS are both ~ 1.22 . Taking the statistical uncertainties into consideration, they are not significantly larger than 1 ($\leq 1.8\sigma$). It is also comforting to note that the best-fit $\epsilon - 1$ values are only half of a fractional bin width of the ground-based instruments' data. Therefore, we have obtained physically reasonable fits.

It turns out that the photon index Γ for $P1_M$ is lower than that for the full phase by only $\sim 1.2\sigma$, while Γ for $P2_M$ is lower than those for $P1_M$ and the full phase by $\sim 2.1\sigma$ and $\sim 3.6\sigma$ respectively. In other words, as the photon energy increases from 10 GeV to ~ 1 TeV, the fractional flux of P1 remains constant or even slightly rises back, and that of P2 is significantly rising. The validity of the trend (e) is still suggested at energies > 10 GeV. Since the fluxes of LW1 and TW2 account for a negligibly small fraction of $\leq 6\%$ (at a 95% confidence level) above 10 GeV, the rise in total fractional flux of P1 and P2 implies a decline in total fractional flux of TW1, BD and LW2. This strengthens the interpretation that the trend (f) is reversed.

4. Discussion and conclusion

Our pulse profiles, wavelet transformations and spectral analyses for the Crab pulsar both demonstrate the strong dependence of the pulse shape on the photon energy, confirming previous studies. Equivalently, the LAT spectral shape of the Crab pulsar widely varies from phase to phase, indicating multiple origins of γ -ray emissions. According to the change in flux proportion among different phases with energy, the trends (a)–(f) derived in §3.2 are generally valid below 10 GeV.

At any on-pulse phase we investigate, the broadband LAT spectrum of the Crab pulsar exhibits a (sub-)exponential cutoff at $E_c \lesssim 10$ GeV. We observe a higher PLEC cutoff energy at P2 than at P1 for the Crab pulsar. Interestingly, such a trend is predicted to occur for about 75% of cases in the scenario of a dissipative magnetosphere model, where a relatively larger and azimuthally dependent electric field operates outside the light cylinder (Brambilla et al. 2015).

In the framework of Lyutikov (2012) and Lyutikov et al. (2012) for IC emission within the outer gap, the γ -ray spectrum of a pulsar could also manifest itself as a broken power law whose spectral break would correspond to a break in the electron distribution. This prediction is also consistent with a property observed by LAT and ground-based instruments: The Crab pulsar's spectrum from 10 GeV to ~ 1 TeV follows a PL tail.

For the spectrum during the phase 0.04–0.24 (covering the whole BD), λ yielded by PLSEC is ≥ 1 and E_c yielded by PLEC is $\sim (6\text{--}10.5)$ GeV, consistent with an inherent feature (a super-exponential cutoff) predicted in polar cap models (e.g., de Jager

2002; Dyks & Rudak 2004). Such a relatively sharp cutoff is explainable in terms of strong magnetic absorption of low-altitude γ -ray photons above 10 GeV. However, the bridge emission of the Crab pulsar is significantly detected by MAGIC at energies up to 200 GeV (Aleksić et al. 2014). The PL indices of its > 10 GeV LAT spectrum (in this work) and > 50 GeV MAGIC spectrum (Aleksić et al. 2014) are both ~ 4 . This is not expected in polar cap models.

During LW1, P1, P2 and TW2, a sub-exponential cutoff with $\lambda \leq 0.6$ is strongly favoured to describe the observed spectrum. This rules out the polar cap origin and suggests high-altitude emission zones for these phases. While a traditional outer gap model naturally explains the sub-exponential cutoff detected for the Geminga pulsar (Ahnen et al. 2016), it can only account for the emissions of the Crab pulsar at energies no higher than 10 GeV. The Crab pulsar's spectrum at each pulse peak exhibits a > 10 GeV PL tail (in this work) which is much harder than that of the Geminga pulsar (Ahnen et al. 2016), and the tail for P2 even extends to 1.5 TeV without a spectral break (Ansoldi et al. 2016). Therefore, a more complicated scenario is required to explain the spectral properties of the Crab pulsar at P1 and P2.

The IC γ -rays (including SSC emission) from magnetospheric acceleration gaps, with “ad hoc” modifications to the models, can roughly match the P1 and P2 fluxes of the Crab pulsar at energies up to 400 GeV (e.g., Aleksić et al. 2011, 2012; Harding & Kalapotharakos 2015; Osmanov & Rieger 2017). Impressively, Harding & Kalapotharakos (2015) took into account the primarily accelerated electrons as well as the leptonic pairs generated by cascades, and Osmanov & Rieger (2017) considered magnetocentrifugal particle acceleration which is efficient close to the light cylinder. Proposed feasible alternatives include wind models, where pulsed γ -rays are due to synchrotron and/or IC radiation from relativistic electrons outside the light cylinder. Aharonian et al. (2012) modelled the pulsed γ -ray emission of the instantaneously accelerated wind, while Arka & Dubus (2013) and Mochol & Petri (2015) modelled that of the wind current sheet.

The trends (a) and (d) of the Crab pulsar entail a decrease in pulse width with increasing energy, which is also detected for the Vela pulsar (DeCesar 2013; H. E. S. S. Collaboration et al. 2018). Such a phenomenon is naturally explained by wind models as well. Besides, a harder spectrum at P2 compared to P1 (i.e., the trend (e)) is observed for both Crab and Vela pulsars (this work; DeCesar 2013; H. E. S. S. Collaboration et al. 2018). This could be attributed to an anisotropy of the wind (Aharonian et al. 2012). Furthermore, wind models predict the bridge emission above 50 GeV as well, but a more complicated density profile of the wind is required to reproduce the observed flux proportion among the bridge and two peaks (Aharonian et al. 2012; Khangulyan et al. 2012).

For the phase-averaged spectrum in GeV–TeV, a schematic comparison of observational results with different theoretical predictions is shown in Figure 10. Both of the two outer gap models, established by Aleksić et al. (2012) and Harding & Kalapotharakos (2015) respectively, fail to describe the spectral shape observed in 1–10 GeV. The sum of the freshly-accelerated wind's IC emission modelled by Aharonian et al. (2012) and the extrapolation of our PLSEC model can account for the γ -ray spectrum up to ~ 400 GeV. This implies that our PLSEC can be interpreted as a nominal component (i.e., synchro-curvature radiation from the outer gap and/or wind). On the other hand, Mochol & Petri (2015) established a model for a current sheet of striped wind which can, in absence of an outer-gap component, satisfactorily reproduce the observed flux and spectral

Table 4. Joint fits of the LAT and ground-based instruments' spectral points for the Crab pulsar at different phases. The PLSF model is assumed.

Phase	Instruments	N_0^a ($10^{-12} \text{ cm}^{-2} \text{ s}^{-1} \text{ GeV}^{-1}$)	Γ	ϵ	$\chi^2/d.o.f.$
Full-phase	LAT & VERITAS	3.0 ± 0.5	3.41 ± 0.12	1.22 ± 0.12	3.1/6
$P1_M$	LAT & MAGIC	16.9 ± 2.9	3.20 ± 0.13	1.23 ± 0.14	8.6/14
$P2_M$		18.5 ± 2.6	2.85 ± 0.10		

^a It has been scaled by the inverse of the phase interval.

shape from 1 GeV to 1 TeV. In this model, the transition from the synchrotron-dominated spectrum to the SSC-dominated spectrum occurs at ~ 300 GeV.

All in all, we propose a hybrid scenario where different acceleration sites account for pulsed γ -rays of the Crab pulsar at different phases and energies. Roughly speaking, the polar cap is responsible for the emission at and around the bridge below 10 GeV, the outer gap is responsible for <10 GeV emissions at other phases, and the wind is responsible for emissions above 10 GeV at any phase. In a more detailed modelling approach, one should carefully deal with the transition phases and transition energies among different emission components.

Acknowledgements. PKHY acknowledges the support of the DFG under the research grant HO 3305/4-1. PKHY gives sincere gratitude to D. Horns for useful discussions and for his encouragement regarding my submission as a single author. We greatly appreciate M. Kerr for providing the ephemeris of the Crab pulsar for phased analysis. We thank D. Carreto Fidalgo for his help in reconstructing Figure 10. We thank the anonymous referee for very useful comments which helped to improve the manuscript.

Lyutikov, M. 2012, ApJ, 757, 88
 Lyutikov, M., Otte, N., & McCann, A. 2012, ApJ, 754, 33
 Mochol, I. & Petri, J. 2015, MNRAS, 449, L51
 Muslimov, A. G. & Harding, A. K. 2004, ApJ, 606, 1143
 Nguyen, T. & VERITAS Collaboration. 2015, in International Cosmic Ray Conference, Vol. 34, 34th International Cosmic Ray Conference (ICRC2015), 828
 Osmanov, Z. & Rieger, F. M. 2017, MNRAS, 464, 1347
 Romani, R. W. 1996, ApJ, 470, 469
 Romani, R. W. & Yadigaroglu, I. A. 1995, ApJ, 438, 314
 Sturrock, P. A. 1971, ApJ, 164, 529
 Takata, J., Shibata, S., Hirotani, K., & Chang, H. K. 2006, MNRAS, 366, 1310
 Tang, A. P. S., Takata, J., Jia, J. J., & Cheng, K. S. 2008, ApJ, 676, 562
 The Fermi-LAT collaboration. 2019, arXiv e-prints, arXiv:1902.10045
 VERITAS Collaboration, Aliu, E., Arlen, T., et al. 2011, Science, 334, 69
 Yeung, P. K. H. & Horns, D. 2020, arXiv e-prints, arXiv:2004.03562

References

- Abdo, A. A., Ackermann, M., Ajello, M., et al. 2010, ApJ, 708, 1254
 Abdo, A. A., Ajello, M., Allafort, A., et al. 2013, The Astrophysical Journal Supplement Series, 208, 17
 Aharonian, F. A. & Bogovalov, S. V. 2003, New A, 8, 85
 Aharonian, F. A., Bogovalov, S. V., & Khangulyan, D. 2012, Nature, 482, 507
 Ahnen, M. L., Ansoldi, S., Antonelli, L. A., et al. 2016, A&A, 591, A138
 Aleksić, J., Alvarez, E. A., Antonelli, L. A., et al. 2012, A&A, 540, A69
 Aleksić, J., Alvarez, E. A., Antonelli, L. A., et al. 2011, ApJ, 742, 43
 Aleksić, J., Ansoldi, S., Antonelli, L. A., et al. 2014, A&A, 565, L12
 Ansoldi, S., Antonelli, L. A., Antoranz, P., et al. 2016, Astronomy and Astrophysics, 585, A133
 Arka, I. & Dubus, G. 2013, A&A, 550, A101
 Arons, J. 1983, ApJ, 266, 215
 Bogovalov, S. V. & Aharonian, F. A. 2000, MNRAS, 313, 504
 Brambilla, G., Kalapotharakos, C., Harding, A. K., & Kazanas, D. 2015, ApJ, 804, 84
 Buehler, R., Scargle, J. D., Blandford, R. D., et al. 2012, The Astrophysical Journal, 749, 26
 Cheng, K. S., Ho, C., & Ruderman, M. 1986, ApJ, 300, 500
 Cheng, K. S., Ruderman, M., & Zhang, L. 2000, ApJ, 537, 964
 Daugherty, J. K. & Harding, A. K. 1982, ApJ, 252, 337
 de Jager, O. C. 2002, Bulletin of the Astronomical Society of India, 30, 85
 DeCesar, M. E. 2013, PhD thesis, University of Maryland, College Park
 Dyks, J. & Rudak, B. 2003, ApJ, 598, 1201
 Dyks, J. & Rudak, B. 2004, Advances in Space Research, 33, 581
 Fierro, J. M., Michelson, P. F., Nolan, P. L., & Thompson, D. J. 1998, ApJ, 494, 734
 H. E. S. S. Collaboration, Abdalla, H., Aharonian, F., et al. 2018, A&A, 620, A66
 Harding, A. K. & Kalapotharakos, C. 2015, ApJ, 811, 63
 Harding, A. K., Kalapotharakos, C., Barnard, M., & Venter, C. 2018, ApJ, 869, L18
 Harding, A. K., Tademaru, E., & Esposito, L. W. 1978, ApJ, 225, 226
 Khangulyan, D., Aharonian, F. A., & Bogovalov, S. V. 2012, in American Institute of Physics Conference Series, Vol. 1505, American Institute of Physics Conference Series, ed. F. A. Aharonian, W. Hofmann, & F. M. Rieger, 29–36
 Lobanov, A. P., Horns, D., & Muxlow, T. W. B. 2011, Astronomy and Astrophysics, 533, A10

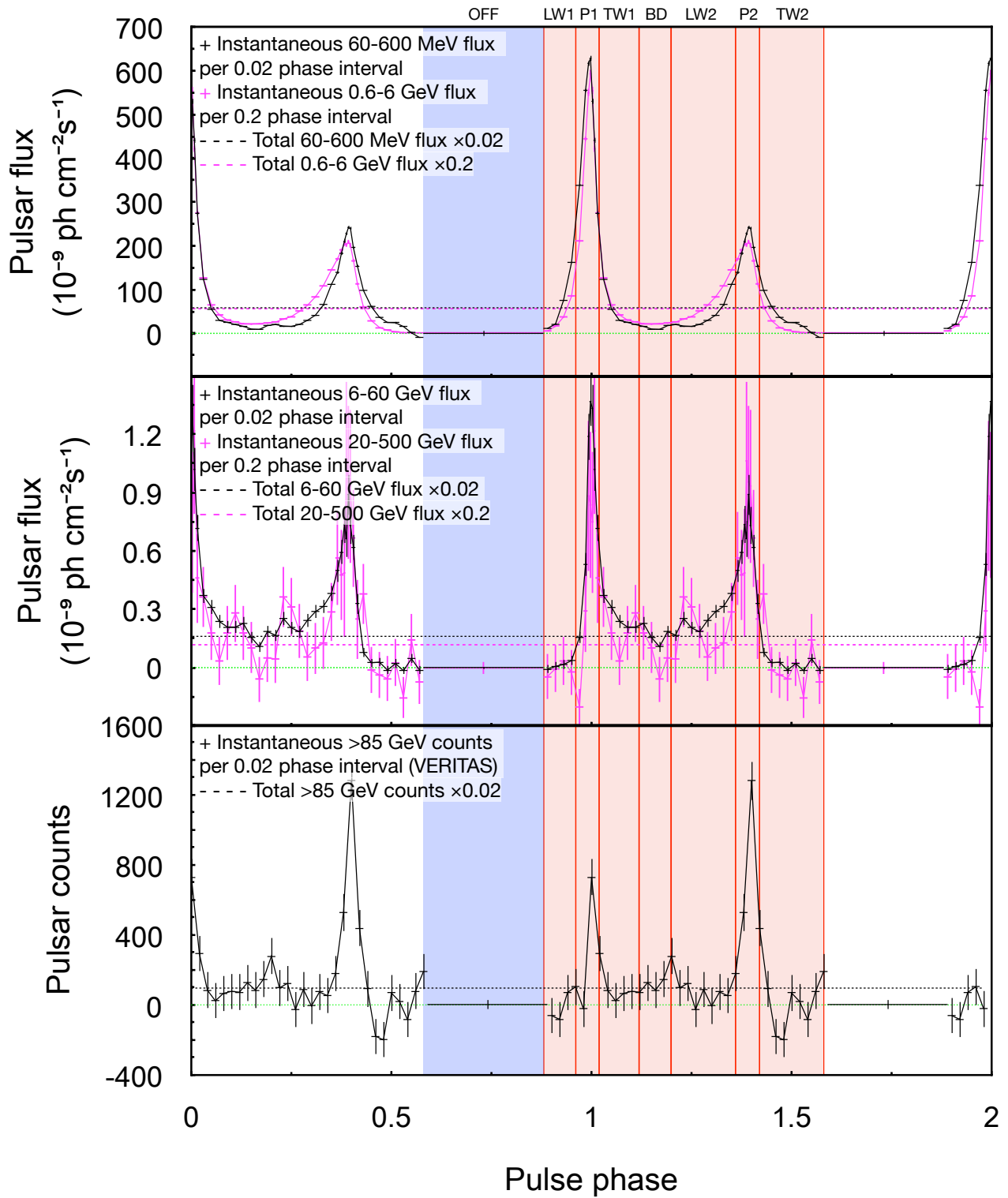


Fig. 1. Phaseograms of the Crab pulsar in different energy bands. The >85 GeV phaseogram observed by VERITAS (the bottom panel) is taken from Nguyen & VERITAS Collaboration (2015).

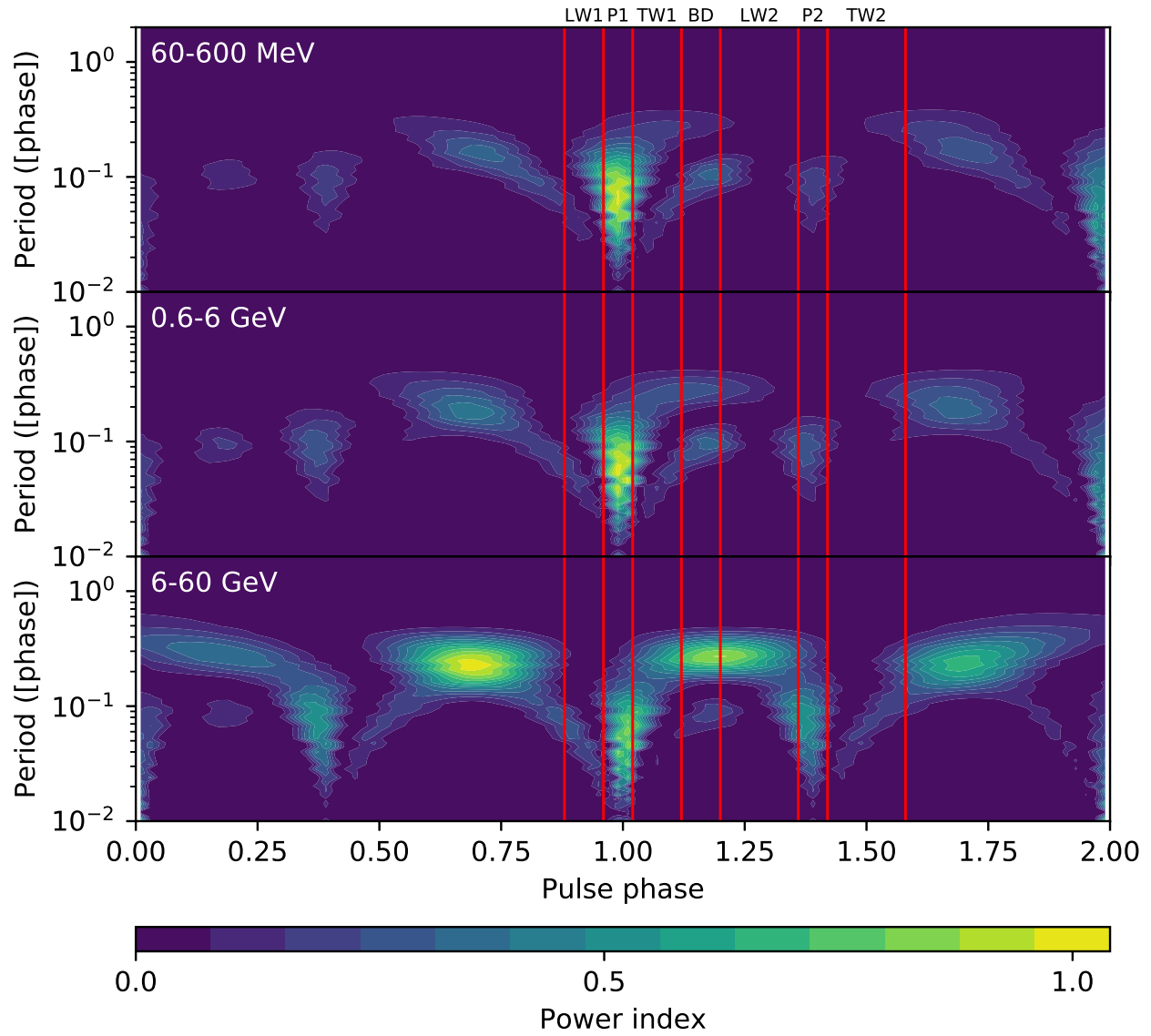


Fig. 2. Wavelet maps of the preliminary LAT phaseograms in three exclusive energy bands. A continuous Fourier transform is applied in the period domain for each phaseogram. The Ricker wavelet is adopted. The power index (the colour scale) is defined as the variance per unit period per unit phase divided by the maximum. Each red vertical line is a border between two phase ranges we define.

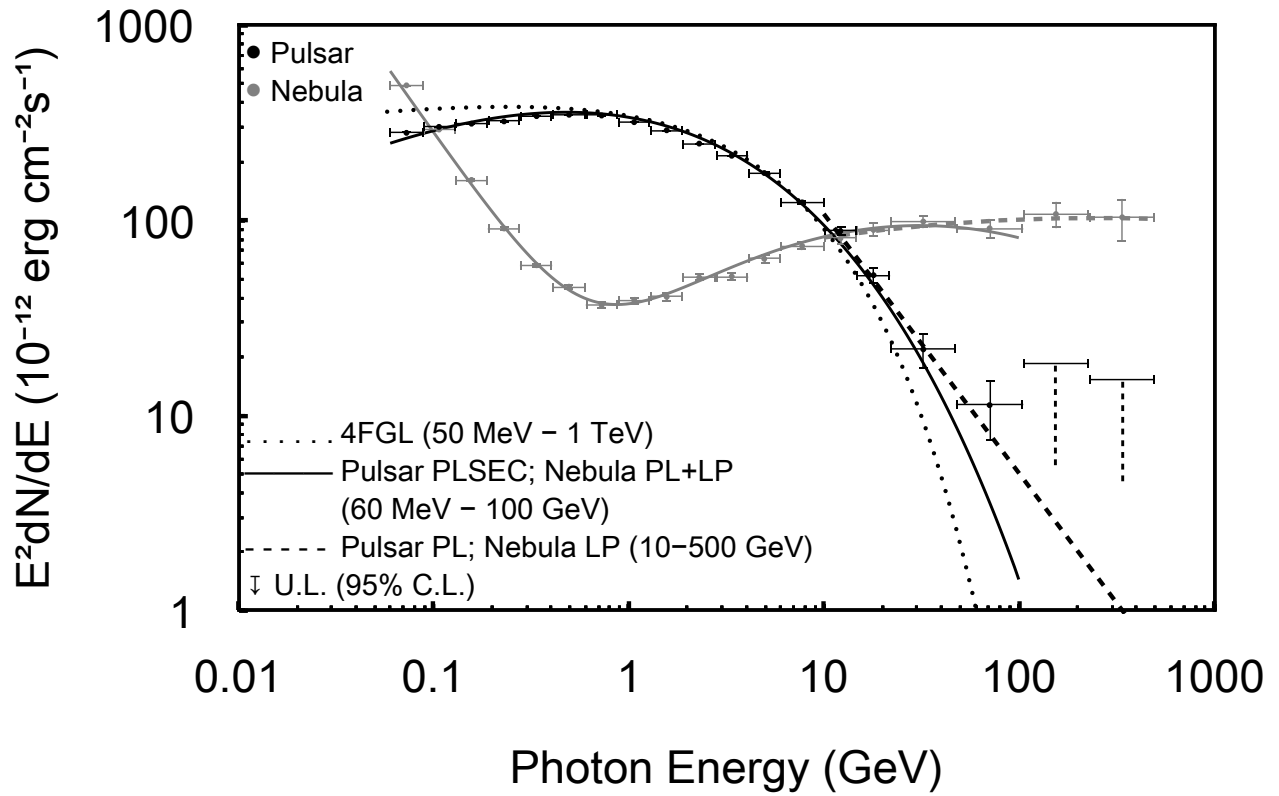


Fig. 3. Phase-averaged LAT SEDs of the Crab pulsar and the Crab Nebula. The 4FGL model for the Crab pulsar, reconstructed with fixing λ at $2/3$, is overlaid for comparison. All upper limits presented are at a 95% confidence level. We overlay the 60 MeV–100 GeV spectrum predicted by PLSEC and the 10–500 GeV spectrum predicted by PL.

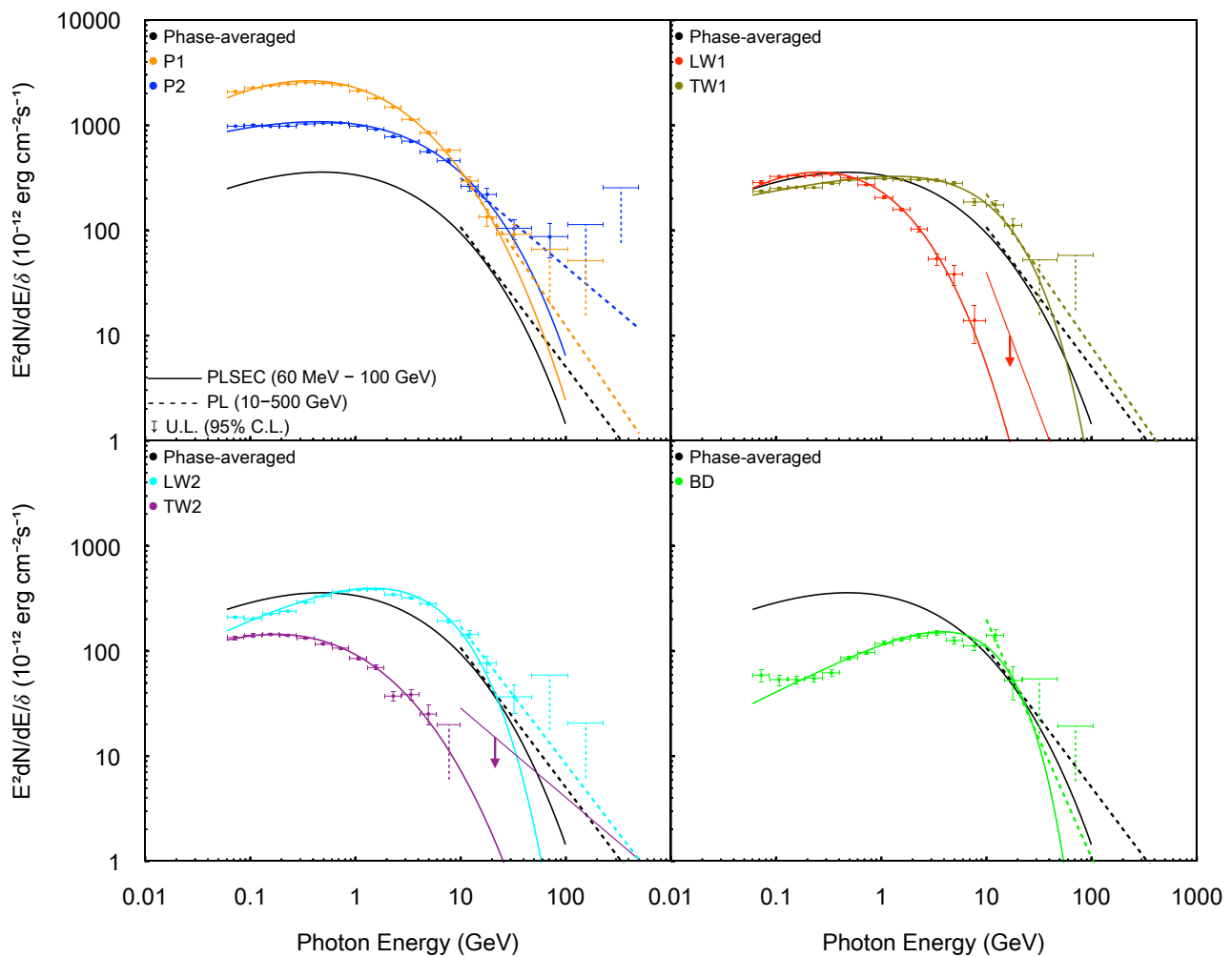


Fig. 4. Phase-resolved LAT SEDs of the Crab pulsar. The vertical axis of each panel shows the differential flux per unit phase (δ). All upper limits presented are at a 95% confidence level. For each phase we investigate, we overlay the 60 MeV–100 GeV spectrum predicted by PLSEC and the 10–500 GeV spectrum predicted by PL. The model lines fit to the phase-averaged pulsar spectrum (Figure 3) are also overlaid on each panel for comparison. Since the Crab pulsar is not significantly detected ($< 2\sigma$) above 10 GeV at LW1 and TW2, the upper limits on differential fluxes at these energies and phases are represented by “ad hoc” PL models (the red and purple straight lines appended with arrows), each of which is determined through iterating the prefactor while fixing the index at the maximum-likelihood value.

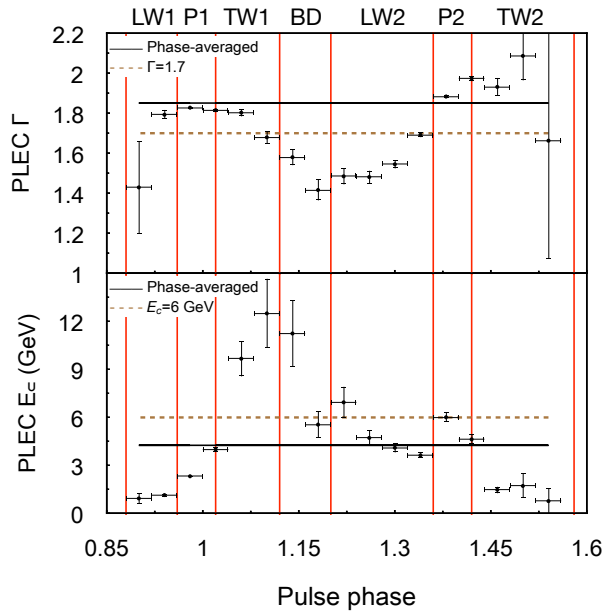


Fig. 5. Photon indices Γ and cutoff energies E_c yielded by PLEC for individual phase bins of 0.04.

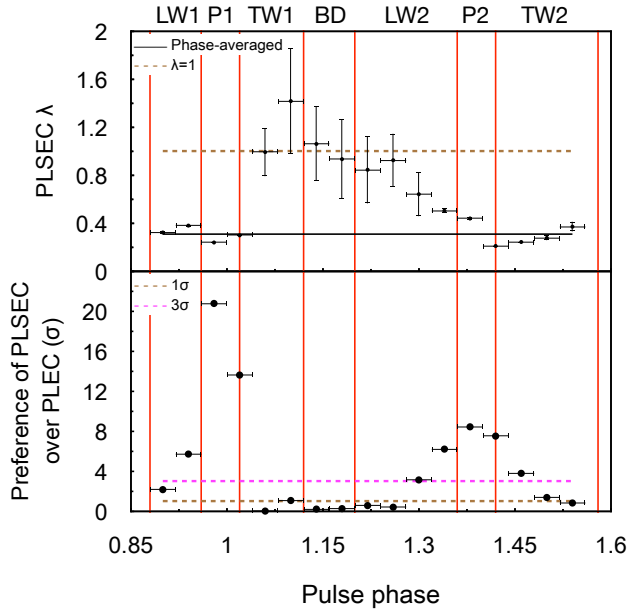


Fig. 6. λ values yielded by PLSEC and preference of PLSEC over PLEC for individual phase bins of 0.04. The latter is computed as the square root of the TS difference between those two models.

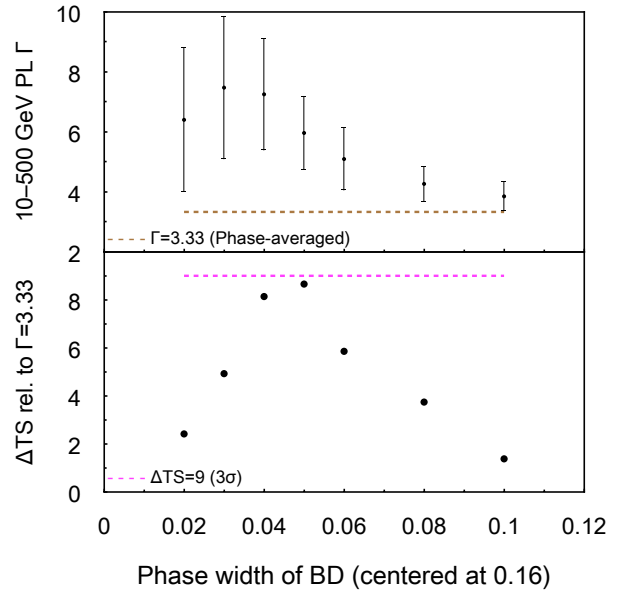


Fig. 7. (top) Evolution of the 10–500 GeV PL index Γ with adjustments to the phase width of BD. (bottom) Corresponding TS differences between fixing Γ at the phase-averaged value of 3.33 and leaving it free. Each of their square roots is the significance at which the local spectrum for an adjusted phase interval of BD is softer than the phase-averaged spectrum.

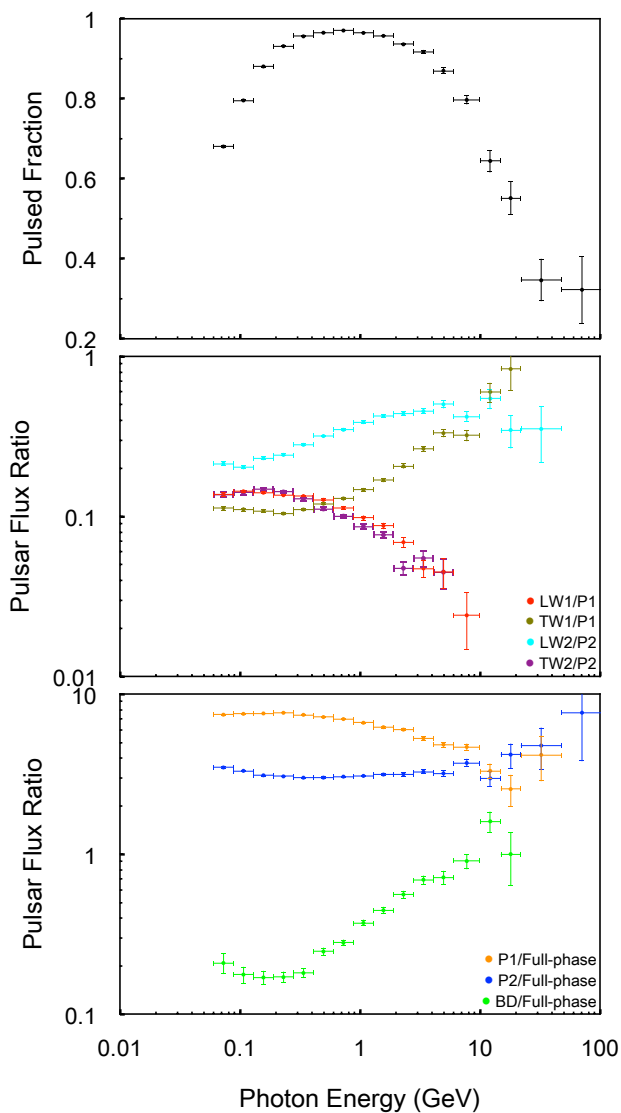


Fig. 8. (top) Pulsed fraction of the entire Crab pulsar/nebula complex. (middle & bottom) Flux ratios of the Crab pulsar between different pairs of phases in different energy bins. We recall that each flux has been scaled by the inverse of the phase interval.

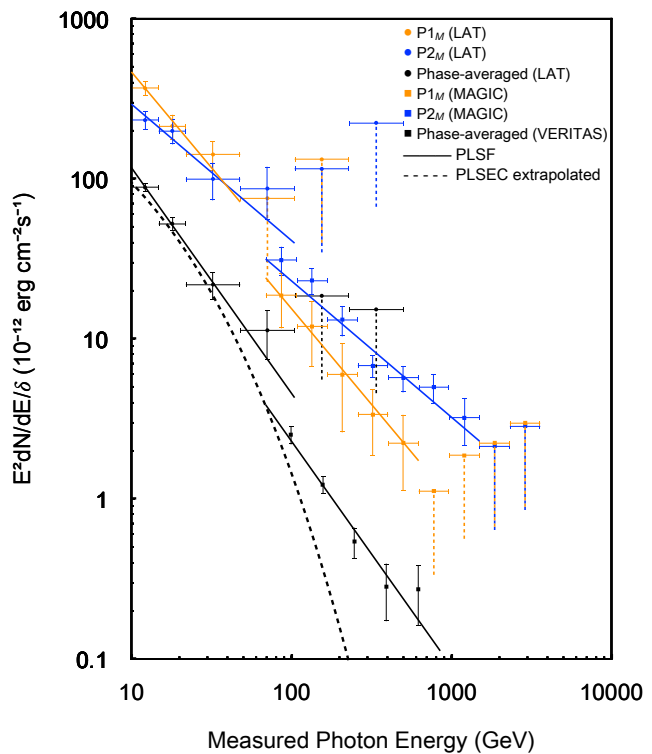


Fig. 9. >10 GeV SEDs of the Crab pulsar at different pulse phases observed with LAT and ground-based instruments. The vertical axis shows the differential flux per unit phase (δ). The horizontal axis shows the measured photon energy (unscaled). Be noted that the orange/blue LAT bins presented here are different from those presented in Figure 4 because the phase ranges are adjusted for comparison purpose. For each phase we investigate, we overlay the spectrum predicted by the joint-instrument fit of PLSF. The PLSEC fit to the broadband LAT spectrum in the full phase (Figure 3) and its extrapolation are also overlaid for comparison.

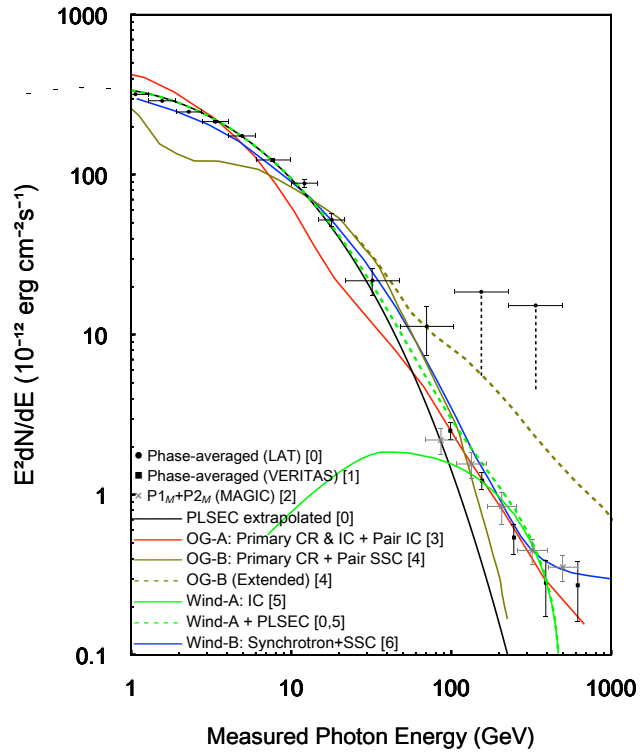


Fig. 10. Comparison of the observed full-phase spectrum with four theoretical models, namely OG-A, OG-B, Wind-A and Wind-B. Descriptions of points and lines are at the bottom-left corner. OG stands for “outer gap”. CR stands for “curvature radiation”. “Primary” means emission from primarily accelerated electrons. “Pair” means emission from leptonic pairs generated by cascades. “OG-B (Extended)” is the nominal OG-B model modified with a power-law extension to the cascade pair spectrum. References: [0] this work, [1] Nguyen & VERITAS Collaboration (2015), [2] Ansoldi et al. (2016), [3] Aleksić et al. (2012), [4] Harding & Kalapotharakos (2015), [5] Aharonian et al. (2012), [6] Mochoł & Petri (2015).

Inferring the origins of the pulsed γ -ray emission from the Crab pulsar with ten-year *Fermi* LAT data (Corrigendum)

Paul K. H. Yeung^{1,2}

¹ Institute of Experimental Physics, Department of Physics, University of Hamburg, Luruper Chaussee 149, D-22761 Hamburg, Germany
e-mail: kin.hang.yeung@desy.de

² Nicolaus Copernicus Astronomical Center, Polish Academy of Sciences, Radańska 8, 87-100, Toruń, Poland

March 12, 2021

ABSTRACT

A&A 640, A43 (2020), <https://doi.org/10.1051/0004-6361/202038166>

Key words. pulsars: individual: Crab pulsar – gamma rays: stars

This is a corrigendum to the original article Yeung (2020) and is mostly adapted from Appendix C.4 of the author's PhD thesis (Yeung 2021).

In Section 3.4 of the original article, we deduced from the "power law with a scaling factor" (PLSF) fitting result that Γ for $P2_M$ is lower than that for $P1_M$. Nevertheless, the previous calculation of the significance of this difference did not consider the covariance of the Γ values for $P1_M$ and $P2_M$ (be noted that the spectral data for $P1_M$ and $P2_M$ are fit simultaneously such that their solutions share the same scaling factor ϵ). After taking this covariance into account, which is computed to be 0.010, we now determine that Γ for $P2_M$ is lower than that for $P1_M$ by 0.35 ± 0.08 , which corresponds to $\sim 4.2\sigma$ (much higher than the $\sim 2.1\sigma$ reported in the original paper). Additionally, Figure 1 demonstrates that the 4σ confidence region of Γ values for $P1_M$ and $P2_M$ excludes all equal-value combinations.

The revised significance strengthens the argument that the flux ratio of $P1$ to $P2$ still decreases with photon energy even above 10 GeV. This, in turn, strengthens the interpretation that there are anisotropic pulsar winds that could lead to the observed harder spectrum at $P2_M$ relative to $P1_M$ (as put forward by Aharonian et al. 2012).

Moreover, taking the statistical errors into account, the ϵ values obtained for MAGIC and VERITAS (both ~ 1.22) are basically consistent with the estimated systematic errors of around 15% on energy scales of IACT telescopes under perfect atmospheric conditions (e.g., Aharonian et al. 2006; Aleksić et al. 2016). This provides further confirmation for the physical reasonableness of those fitting results.

References

- Aharonian, F., Akhperjanian, A. G., Bazer-Bachi, A. R., et al. 2006, A&A, 457, 899
Aharonian, F. A., Bogovalov, S. V., & Khangulyan, D. 2012, Nature, 482, 507
Aleksić, J., Ansoldi, S., Antonelli, L. A., et al. 2016, Astroparticle Physics, 72, 76
Yeung, K. H. 2021, PhD thesis, Staats-und Universitätsbibliothek Hamburg Carl von Ossietzky

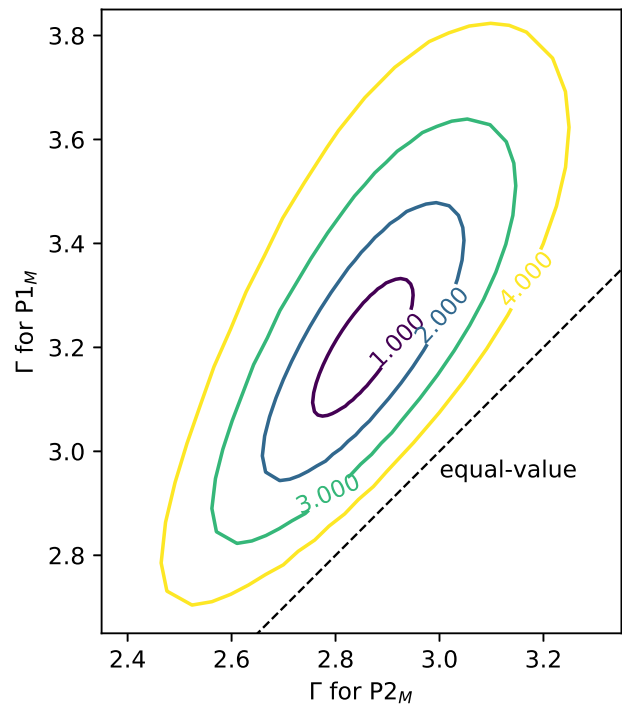


Fig. 1. Confidence regions of Γ values for $P1_M$ and $P2_M$. The plotted covariance contours respectively correspond to the significance levels of 1σ , 2σ , 3σ , and 4σ (from innermost to outermost). The reference line (which is black, dashed, and straight) indicates the combinations of equal Γ values.

Yeung, P. K. H. 2020, A&A, 640, A43

arXiv:2004.07669v3 [astro-ph.HE] 10 Mar 2021